IPEM
Institute of Physics and
Engineering in Medicine

PAPER • OPEN ACCESS

Suitability of low density materials for 3D printing of physical breast phantoms

To cite this article: Danail Ivanov *et al* 2018 *Phys. Med. Biol.* **63** 175020

View the article online for updates and enhancements.

You may also like

Physics in Medicine & Biology

IPEM Institute of Physics and Engineering in Medicine

PAPER

Suitability of low density materials for 3D printing of physical breast phantoms

Danail Ivanov[1], Kristina Bliznakova[1], Ivan Buliev[1], Peycho Popov[1], Giovanni Mettivier[2], Paolo Russo[2], Francesca Di Lillo[2], Antonio Sarno[2], Janne Vignero[3], Hilde Bosmans[3], Alberto Bravin[4] and Zhivko Bliznakov[1]

[1] Laboratory of Computer Simulations in Medicine, Technical University of Varna, Varna, Bulgaria
[2] Dipartimento di Fisica 'Ettore Pancini', and INFN Sezione di Napoli, Università di Napoli Federico II, Napoli, Italy
[3] Department of Radiology, Medical Imaging Research Center, University Hospitals Leuven, Herestraat 49, 3000 Leuven, Belgium
[4] European Synchrotron Radiation Facility (ESRF), Grenoble F-38043, France

E-mail: kristina.bliznakova@tu-varna.bg and kristina.bliznakova@gmail.com

Abstract

Breast physical phantoms are a basic tool for the assessment and verification of performance standards in daily clinical practice of x-ray breast imaging modalities. They are also invaluable in testing and evaluation of new x-ray breast modalities to be potentially established, e.g. breast computed tomography, dual-energy breast CT and phase-contrast mammography and tomography. Nowadays, there is a lack or there are only a limited number of breast physical phantoms available for this purpose.

The aim of this study is to explore a range of 3D printing materials such as resins, PLA, ABS, Nylon etc, to determine their attenuation and refractive properties, and to finally compare them to the properties of the breast tissues: adipose, glandular and skin.

To achieve this goal, step-wedge phantoms were computationally modeled and then manufactured using stereolithographic and fused-deposition modeling technologies. X-ray images of the phantoms were acquired, using monochromatic beam at ID17, ESRF, Grenoble for three energies—30 keV, 45 keV and 60 keV. Experimental data were further processed to obtain the linear attenuation coefficients of these materials. Comparison with theoretical data for the linear attenuation coefficients and the refractive indexes for breast tissues was performed.

From the studied materials, most of the resins, Nylon, Hybrid, PET-G show absorption properties close to the glandular tissue, while ABS shows absorption characteristics close to these of the adipose tissue. For phase-contrast imaging, it turns out that the ABS combined with resin-based materials to represent the adipose and glandular tissues, respectively may be a good combination for manufacturing of a phantom suitable for these studies.

These results can be used for the design and the construction of a new physical anthropomorphic phantom of the breast with improved anatomical and radiological characteristics dedicated for advanced mammography imaging techniques implemented at higher photon energies.

1. Introduction

In breast imaging, physical breast phantoms are a basic tool used to assess imaging performance of x-ray breast imaging systems and to evaluate the entrance air kerma or absorbed dose and their conversion to mean glandular dose. Another application of such phantoms is in testing, evaluation and clarification of the role and the benefits of new x-ray modalities in comparative studies to actual daily routine. Breast tomosynthesis (Sechopoulos 2013), contrast-enhanced mammography (Francescone *et al* 2014, Daniaux *et al* 2015), as well as new imaging modalities to be potentially established like breast computed tomography (CT) (Lindfors *et al* 2008, Mettivier and Russo 2011, Kalender *et al* 2012, Sarno *et al* 2015), dual-energy breast CT (Badr *et al* 2014) and phase-contrast breast imaging (Bravin *et al* 2013, Auweter *et al* 2014, Sarno *et al* 2017a) are being explored.

Most physical breast phantoms (as opposed to digital phantoms, (Mettivier *et al* 2017)) have a homogeneous background with inserted test objects approximating lesions. These phantoms are not used for routine quality

assurance procedures nowadays and this explains the limited number of physical breast phantoms commercially available. For research purposes, many of the existing phantoms should be developed to a next degree of sophistication. A complete review of physical phantoms used in mammography is available from Tomal *et al* (2014).

The most used materials for the production of such phantoms are resins and polymethyl methacrylate (PMMA), the later not being a printing material. Among the commercially available physical anthropomorphic phantoms, one can mention the 'Rachel' anthropomorphic breast phantom, Gammex 169 and the BR3D breast imaging phantom model 020 as well as the BR3D and the CIRS 073 (www.cirsinc.com/). The Rachel phantom is limited to a use in planar x-ray imaging and currently not available commercially, while the BR3D is manufactured specifically for breast tomosynthesis (Sarno *et al* 2017b). The multi-modality breast biopsy and sonographic trainer CIRS 073 mimics the heterogeneous appearance of breast tissue under various breast imaging modalities, and has cystic and dense lesions embedded within the breast background. However, these phantoms do not reflect a realistic breast tissue anatomy.

Anthropomorphic physical three-dimensional (3D) phantoms are needed and expected to produce a realistic tissue background patterns in the images, important for the investigation of the detectability of lesions, performance of image processing algorithms, reconstruction algorithms or applications such as synthetic two-dimensional (2D) images that capture important features of 3D stacks. More recently, Ikejimba *et al* (2017) reported a method for the creation of realistic, inexpensive physical anthropomorphic phantoms dedicated to use in full field digital mammography and digital breast tomosynthesis. The method is based on a virtual model, materialised in a slice-by-slice process through inkjet printing, using parchment paper and a radiopaque ink containing 33% ($I_{33\%}$) or 25% ($I_{25\%}$) iohexol by volume. Although the proposed method is relatively inexpensive, we believe the future belongs to 3D printing technologies. Amongst the initially developed physical phantoms for research purposes are phantoms developed from 3D software models of breast (Carton *et al* 2011, Bliznakova *et al* 2016), or based on clinical patient data (Kiarashi *et al* 2015). Manufacturing of such phantoms with 3D printers is challenging due to the limitations in the current printing technology, like manufacturing precision and the limited number of printing materials that can be applied simultaneously. The 3D printing is a time-consuming procedure, and it is also true that radiological characteristics of the printing materials have not been studied in details.

To print an anthropomorphic phantom, a digital (software) model is required, which may be obtained either from medical imaging techniques such as MRI, CT, PET or created by using a dedicated (CAD) software. Once the software models are created, they are routinely converted to stereolithography files and printed with 3D printers. Such an approach has been followed by Winslow *et al* (2009) for the production of three different adult anthropomorphic phantoms from original segmented CT patient datasets.

In the field of x-ray breast imaging, few works have been focused on measurements of the attenuation coefficients of materials, which may be used in manufacturing of breast phantoms, by exploiting 3D printing. It was found that for mammography energies (between 22 kV and 32 kV), acrylic-based photopolymers are suitable to mimic the properties of the glandular breast tissue (Carton *et al* 2010). To increase the linear attenuation coefficient of the photopolymer materials, they were doped with concentrations of the nanoscale TiO_2 (Sikaria *et al* 2016) and with calcium, iodine and zinc (Zhao *et al* 2017), and found that zinc-doping can potentially increase attenuation to 100% breast density and beyond. For the same photon energies, the x-ray properties of the materials used by stereolithographic 3D printers were found similar to these of the PMMA (Clark *et al* 2016). Moreover, resins of different colors had very similar x-ray attenuation. For higher photon energies (80 kV and 120 kV), Dancewicz *et al* (2017) concluded that ABS printed samples with an infill density of 90% is a good approximation of adipose tissue, while photoluminescent PLA with infill density of 50% is suitable to reproduce the breast tissue.

Our long-term aim is the development of physical breast phantoms dedicated to studying x-ray imaging of the breast, including advanced techniques such as breast CT, phase-contrast and dual-energy imaging. These techniques are implemented at higher photon energies compared to the mammography x-ray imaging (Bisogni *et al* 2007, Lindfors *et al* 2008, Zhao *et al* 2012, Sarno *et al* 2016, Ghani *et al* 2017, 2018). To successfully design and manufacture such phantoms the properties of the available printing materials need to be investigated. The aim of this study is to determine the radiological characteristics of common 3D printable plastic materials and investigate their suitability as tissue substitutes in physical breast phantoms for x-ray imaging. To the best of our knowledge, the presented work is the most complete in the field of printing materials for low cost 3D printers.

2. Materials and methods

2.1. Reference and studied materials

Normal breast tissue can be considered and described as mainly consisting of adipose, gland and skin tissues. Hence, those tissues are used as reference in the current study. Table 1 give their elemental composition in terms of weight fraction, and the composition of several materials often used in the fabrication of breast physical phantoms as breast substitutes, as well as commonly used 3D printing materials.

Table 1. Elemental composition and density of breast tissues, substitutes and 3D materials.

Tissue/material	H	C	N	O	Na	P	S	Cl	K	Density g cm^{-3}
Adipose tissue[a]	0.112	0.619	0.017	0.251		0.001				0.93
Gland[a]	0.102	0.184	0.032	0.677		0.005				1.04
Skin[a]	0.098	0.178	0.050	0.667		0.007				1.09
BR12[b]	0.087	0.699	0.024	0.179				0.001		0.97
PMMA[b]	0.080	0.600		0.320						1.19
Polyethylene[b]	0.144	0.856								0.93
Paraffin wax[b]	0.149	0.851								0.93
Polycarbonate[b]	0.055	0.756		0.189						1.20
Liquid water[b]	0.112			0.888						1.00
Nylon[c]	0.099	0.626	0.119	0.156						1.18
PLA[c]	0.053	0.519		0.426			0.001		0.001	1.29
ABS[c]	0.075	0.855	0.053	0.016			0.001			1.09
PET-G[c]	0.075	0.652		0.271			0.002			1.30

[a] Hammerstein *et al* (1979).
[b] Berger *et al* (2010).
[c] Alssabbagh *et al* (2017).

Breast tissue reference data (adipose, gland and skin) in terms of elemental composition were taken from Hammerstein *et al* (1979). Sources of breast tissue data are also available by other authors (Johns and Yaffe 1987, Chen *et al* 2010) but data from Hammerstein are based on the elemental composition which allows calculation of the attenuation coefficients for any x-ray energy. Data for PMMA, polyethylene, paraffin wax, polycarbonate and liquid water were taken from NIST database (Berger *et al* 2010), while these for BR12 from White *et al* (1978). Data for Nylon, PLA, ABS, PET-G were taken from Alssabbagh *et al* (2017).

The materials, evaluated in the current study are listed in table 2. Seventeen of them are used by the 3D printing technology. The selection of those materials was based on the fact that they are common, inexpensive and largely available on the market. The first seven materials (ABS, Brick, Hybrid, Nylon, PET-G, PLA and PVA) are thermoplastic polymers used by Fused Deposition Modelling (FDM) printing technology. They are available in the form of a wire spool. Materials 8-17 (Black, Clear, Flex, Gray, NDBase, NDC + B, NDCast, NDSG, Tough, White) are polymer resins in a liquid form and are used with stereolithography (SLA) technology. They have different properties and are used in diverse applications, such as dental medicine, aerospace, optical prototyping, etc.

In order to study the x-ray properties of the selected materials, three sizes of step-wedge phantoms (scale S, M and L) (figure 1(a)) were manufactured with the help of three 3D printers. Designspark Mechanical software (www.rs-online.com/designspark/mechanical-software) was used to design the models. The dimensions of the step wedge phantoms are specified in the insert of figure 1(a). The size of each step area was made large enough in order to have high number of pixels on the x-ray projection images, necessary for averaging the calculations of the linear attenuation coefficients over the sample surface area. The unknown material density was determined experimentally—the weights of the samples were measured with the precise digital scale equipment (0.01 g) (figure 1(b)), while the volumes were calculated using the Archimedes' principle (measuring the weight of the water, displaced from the sample figure 1(c)). The volume of the PVA, denoted by * in table 2 was measured with a gauge, because the PVA material is soluble in water. The calculated density for each material is shown in table 2.

Well-known PMMA material in slabs of thickness of 1 cm was included in the study for validation of the experimental procedure for determination of the linear attenuation coefficient of the materials. Finally, step-wedges from other three materials of interest (Paraffin and Double Silicon and Gelatin) were manufactured by using a casting technology.

2.2. Experimental setup

The linear attenuation coefficients μ of the investigated materials were determined from x-ray projection data acquired at the biomedical imaging beamline ID17, ESRF, Grenoble. The beam width and height, defined by a slit system placed in front of the sample, were 100 mm and 7 mm, correspondingly. The arrangement for this study is schematically shown in figure 2(a). Three photon energies of the incident beam—30 keV, 45 keV, and 60 keV being of interest for phase contrast breast imaging and breast CT were considered and used. The stability of the beam over the time was also taken into account in their selection. Due to the small beam height (7 mm), the

Table 2. List of materials used in the experimental study.

Number	Substitute	Abbreviation	Printing technology	Density g cm^{-3}
1	ABS[a]	Acrylonitrile butadiene styrene	FDM	1.019 ± 0.002
2	Brick[a]	—	FDM	1.232 ± 0.003
3	Hybrid[a]	—	FDM	1.227 ± 0.003
4	Nylon[a]	—	FDM	1.111 ± 0.002
5	PET-G[a]	Polyethylene terephthalate glycol-modified	FDM	1.236 ± 0.003
6	PLA[a]	Polylactic acid	FDM	1.251 ± 0.003
7	PVA[b]	Polyvinyl alcohol	FDM	1.097 ± 0.013[e]
8	Black[b]	—	SLA	1.183 ± 0.002
9	Clear[b]	—	SLA	1.180 ± 0.002
10	Flex[b]	—	SLA	1.137 ± 0.003
11	Gray[b]	—	SLA	1.175 ± 0.002
12	NDBase[c]	—	SLA	1.190 ± 0.004
13	NDC+B[c]	—	SLA	1.194 ± 0.004
14	NDCast[c]	—	SLA	1.206 ± 0.004
15	NDSG[c]	—	SLA	1.190 ± 0.004
16	Tough[b]	—	SLA	1.181 ± 0.003
17	White[b]	—	SLA	1.178 ± 0.002
18	Paraffin			0.907 ± 0.002
19	Double silicon[d]			1.152 ± 0.002
20	PMMA	Polymethyl methacrylate		1.193 ± 0.001
21	Gelatin			—

[a] www.lpfrg.com/en/filament/.
[b] https://formlabs.com/materials/.
[c] http://nextdent.com/products/base/.
[d] http://en.zhermack.com/Technical/Silicones/Duplication/C400820.kl.
[e] Measured with a gauge.

Dimensions of the three step wedge phantoms.

Parameters	Size	D1 mm	D2 mm	D3 mm	H mm	W mm
Step wedge 1	S	2	4	6	20	25/35
Step wedge 2	M	5	10	15	20	25/35
Step wedge 3	L	20	30	40	20	25/35

(a)   (b)   (c)

Figure 1. Step-wedges used in the study: (a) step-wedge phantom design, (b) weight measure of the printed step-wedge phantom from a tough resin and (c) measuring the volume of the printed phantom.
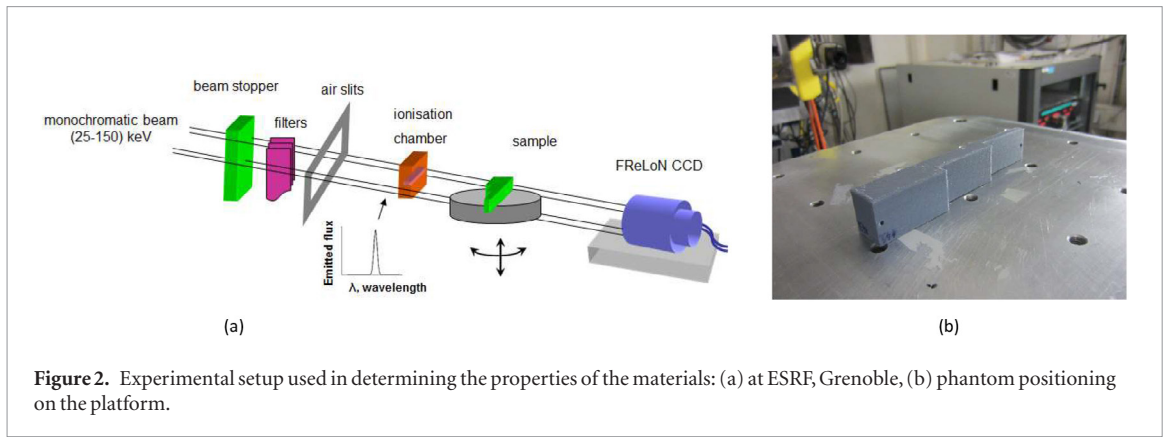
maximum thickness of the sample (4 cm) and the large air gap of 11 m, the influence of the beam width and the scattered radiation on the data was calculated to be negligible (much less than 1%). The incident air kerma was set to values that guarantee good quality of images and low photon noise (1 Gy per image).

The x-ray detector was a high-resolution 'FReLoN' CCD camera with an active input surface of 94 mm × 94 mm (Coan *et al* 2006). The phosphor screen was Gd$_2$O$_2$S:Tb with a thickness of 60 μm. Images were acquired with size of 2048 × 150 pixels, with a pixel size of 46 μm × 46 μm. The distance between the undulator

Figure 2. Experimental setup used in determining the properties of the materials: (a) at ESRF, Grenoble, (b) phantom positioning on the platform.

and the FReLoN camera was 155 m, while the distance between the object and the detector was set to 11 m, for propagation-based phase contrast imaging.

Phantoms were placed on a motorized stage that could perform micrometric movements along the directions: vertical, horizontal and rotational (around a vertical axis). The phantoms were oriented so that the surface of their steps is perpendicular to the incident monochromatic beam (figure 2(b)). The image acquisition for each material comprised three adjacent frames (each of 150 lines), while translating the platform stage vertically. The final projection image was assembled from the three component frames. Each time before taking a frame projection of the phantom, a 'dark-field' reference image I_{dark} was prepared by averaging 100 detector images, taken with closed beam shutter (without radiation). Similarly, a 'flat-field' reference image I_{flat} was obtained by averaging detector images, taken without the presence of the phantom in front of the detector. Each frame image I was next corrected to account for the non-uniformity and the offset of the captured by the detector image intensity:

$$I_{corr} = \frac{I - I_{dark}}{I_{flat} - I_{dark}}. \tag{1}$$

The incident exposure was monitored by a calibrated TW 31010 dosimetry chamber (PTW-Freiburg, Freiburg, Germany), placed horizontally at a distance of 7 m away from the detector surface.

2.3. Calculation and evaluation of μ and δ

The procedure for calculating the linear attenuation coefficients μ based on experimental measurements of the investigated materials was adapted from Heine and Behera (2006) and outlined in figure 4(a). The calculation of the linear attenuation coefficient is based on the Lambert Beer's law. The corrected projection images of three step-wedge phantoms (scale S, M and L) manufactured from Clear resin and PLA are shown in figures 3(a) and (b) for 60 keV energy. The mean value of the transmission in a rectangular region with size of 200×150 pixels was calculated for each material thickness using the freeware ImageJ (https://imagej.nih.gov/ij/). The linear attenuation coefficients were calculated for each material and each energy by least square fitting of a linear model based on the attenuation for nine (within the range from 2 mm to 40 mm) thicknesses as outlined in figure 4(b). The slope of each such line corresponds to the linear attenuation coefficient of the studied material and energy.

The reference data for the monochromatic linear attenuation coefficients were derived from the online version of the XCOM database (Berger *et al* 2010) using the elemental composition from table 1.

In order to validate the linear attenuation coefficients from measurements at ESRF and to calculate the refractive index decrement δ, elemental composition analysis of selected (in regards to their absorption properties to the reference breast tissues) materials was performed using the elemental analyzer EURO EA3000, CHNSO.

The complex refractive index of the material is given by Born and Wolf (1980):

$$n(E) = [1 - \delta(E)] + i\beta(E) \tag{2}$$

where the absorption coefficient β is:

$$\beta(E) = \frac{hc}{4\pi E}\mu(E), \tag{3}$$

h is the Planck constant, and c is the speed of the light. The energy-dependent refractive index decrement $\delta(E)$ can be calculated as:

$$\delta(E) = \frac{\rho_e r_e h^2 c^2}{2\pi E^2} \tag{4}$$

where r_e is the classical electron radius, and ρ_e is the electron density of the material. In this study, the refractive index decrement δ is calculated from equation (4), by using the *XRAYImagingSimulator* (Bliznakova *et al* 2016).
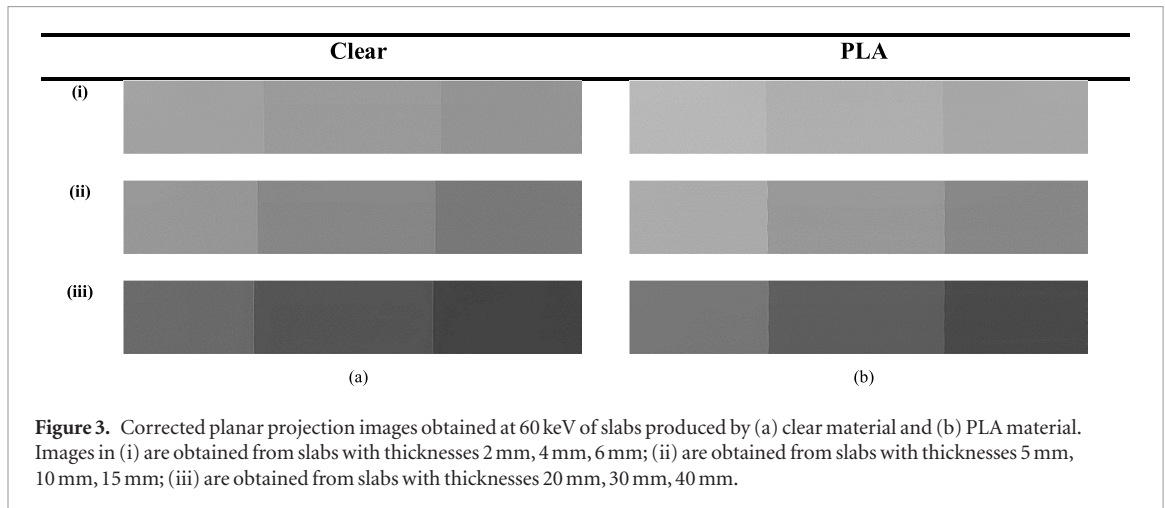
Figure 3. Corrected planar projection images obtained at 60 keV of slabs produced by (a) clear material and (b) PLA material. Images in (i) are obtained from slabs with thicknesses 2 mm, 4 mm, 6 mm; (ii) are obtained from slabs with thicknesses 5 mm, 10 mm, 15 mm; (iii) are obtained from slabs with thicknesses 20 mm, 30 mm, 40 mm.
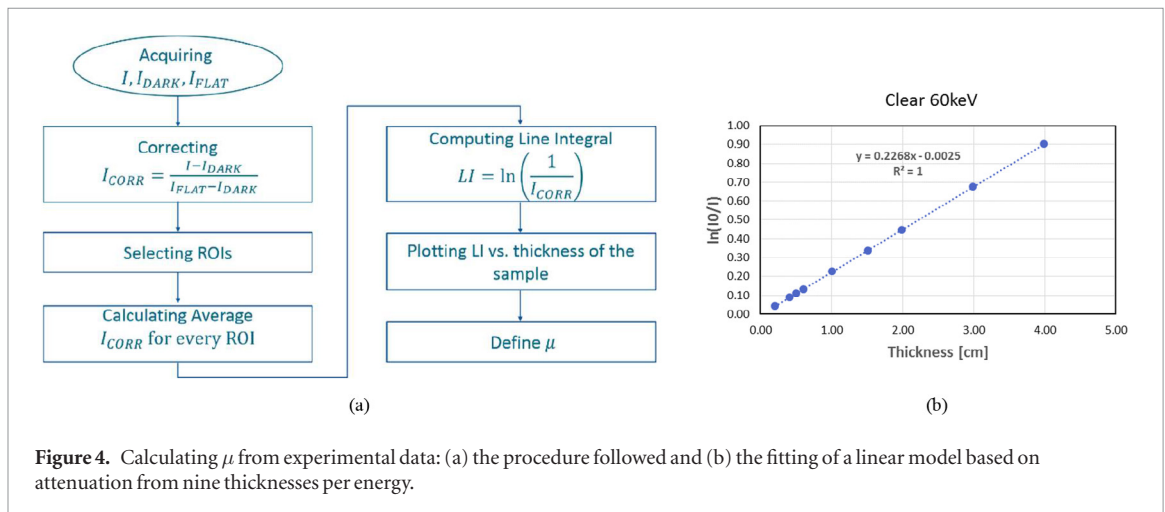

Figure 4. Calculating μ from experimental data: (a) the procedure followed and (b) the fitting of a linear model based on attenuation from nine thicknesses per energy.

The relative difference between the linear attenuation coefficients of any two materials (m_1, m_2) is computed as:

$$\mu_{diff}(m_1, m_2) = \frac{\mu_{m_1} - \mu_{m_2}}{\mu_{m_2}} \times 100, [\%]. \tag{5}$$

Similarly, the relative difference between δ of the same two materials is computed as:

$$\delta_{diff}(m_1, m_2) = \frac{\delta_{m_1} - \delta_{m_2}}{\delta_{m_2}} \times 100, [\%]. \tag{6}$$

In a physical breast phantom, the distribution of adipose, glandular and skin tissues is preliminary determined by its model. To appear more realistic in its x-ray projection images, i.e. to reproduce not only the anatomical structures but also the contrast similar to the one of a real breast, the linear attenuation coefficients of the materials used as tissue substitutes should reflect of the real tissues.

In order to find three materials with linear attenuation coefficients relating to each other as those of adipose, gland and skin, we generated all possible ordered combinations of three materials, i.e. triplets (m_x, m_y, m_z) out of the 21 studied materials (and water) and compared them to a reference triplet of breast tissues $(adipose, gland, skin)$. To estimate the degree of similarity between the triplets of materials (m_x, m_y, m_z) and the reference ones $(adipose, gland, skin)$, the square errors SE_μ and SE_δ were calculated and used:

$$SE_\mu = \sqrt{\left(\mu_{diff}(m_y, m_x) - \mu_{diff}(gland, adipose)\right)^2 + \left(\mu_{diff}(m_z, m_x) - \mu_{diff}(skin, adipose)\right)^2}, [\%] \tag{7}$$

$$SE_\delta = \sqrt{\left(\delta_{diff}(m_y, m_x) - \delta_{diff}(gland, adipose)\right)^2 + \left(\delta_{diff}(m_z, m_x) - \delta_{diff}(skin, adipose)\right)^2}, [\%]. \tag{8}$$

The whole study for estimating the linear attenuation and the refractive decrement index for the selected materials included: (a) validation of the experimental data for the linear attenuation coefficients by comparing the estimated value for PMMA to the corresponding known one; (b) computing of the linear attenuation coefficients of all studied materials and comparing them to the ones of adipose, glandular and skin tissues; (c)

Figure 5. Linear attenuation coefficients μ (cm^{-1}) for the PMMA_NIST, PMMA_LAB and PMMA.
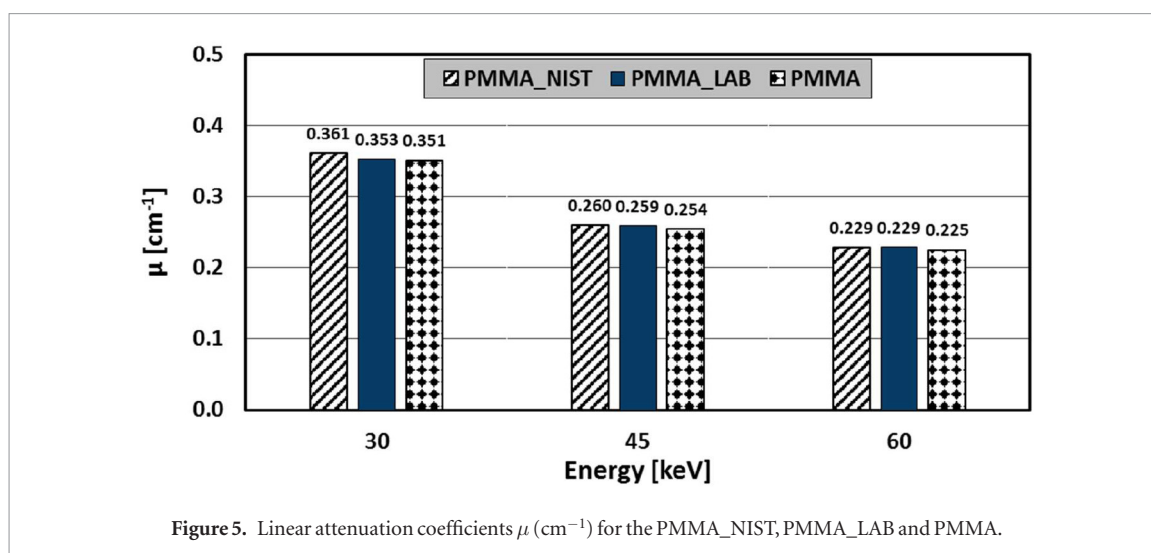
comparison of triplets of linear attenuation coefficients of the studied materials with the corresponding values of the breast tissues and evaluating the suitability of the materials for 3D printing of physical phantoms and (d) additional calculation of the refractive decrement index δ for several materials and estimating their suitability for 3D printing of physical phantoms especially for phase-contrast imaging.

3. Results and discussion

3.1. Validation of the experimental procedure for determining μ

The linear attenuation coefficient for the PMMA derived from NIST database (noted as PMMA_NIST), the one also from NIST database but based on the chemical analysis of the used sample (noted as PMMA_LAB), and the experimentally determined one (PMMA), as outlined in figure 4(a), are plotted in figure 5.

An overall excellent coincidence between measured and calculated linear attenuation coefficients for the PMMA is observed for the three incident energies. The calculated maximum relative difference between measured (PMMA) and calculated from the elemental analysis coefficients (PMMA_LAB) was 1.9% for 45 keV, which confidently confirms the consistency of the approach for estimating the linear attenuation coefficients of the investigated materials. In the same time, the observed difference between PMMA_NIST and PMMA_LAB is less than 2.3% for 30 keV.

3.2. Evaluating of the experimental data for μ

The linear attenuation coefficients of all studied and reference materials for the three energies are summarized in table A1 (in the appendix part). The uncertainties in the computed from measured composition values are in the range $(4\text{--}6) \times 10^{-5}$ and are not reflected in the table. As seen, the linear attenuation coefficients for all materials, except the brick and the double silicon, are within the range of the linear attenuation coefficients of the three breast tissues—adipose, gland and skin. This suggests that these materials may be a suitable choice for manufacturing the main parts of the breast phantoms.

Figure 6 shows the relative difference of linear attenuation coefficients μ of the materials with respect to the one of the glandular tissue. Brick and double silicon were excluded from these comparisons for the reasons mentioned above. The results reveal that the studied resins, all used with stereolithography printing technology, have similar linear attenuation coefficients ($|\mu_{diff}| < 10\%$) compared to the ones of the glandular tissue. In addition, PVA, Hybrid and PET-G, which are used with FDM printing technology, have also attenuation properties close to the properties of the glandular tissue (also $|\mu_{diff}| < 10\%$). Therefore, these materials are considered to represent well the attenuation properties of the gland especially for the energy of 45 keV, as the maximum difference $|\mu_{diff}|$ is 4.67% for Clear resin. The comparison in this figure also suggests that Nylon may be a suitable material to represent the glandular tissue for 45 keV and 60 keV. Amongst the non-printed (casted) materials, gelatin and water show the closest attenuating properties to the glandular tissue, with a maximum difference $|\mu_{diff}|$ of 2.22% for 45 keV energy. The similar linear attenuation values between water and gland were also reported by Poletti *et al* (2002). From these two materials, gelatin is not temperature stable at room temperature conditions and therefore not a preferable material for preparing physical rigid phantoms. Nylon and PVA are both hygroscopic materials, which causes difficulties (i.e. weaker adhesion to the base) during the printing process of the object. Printing and
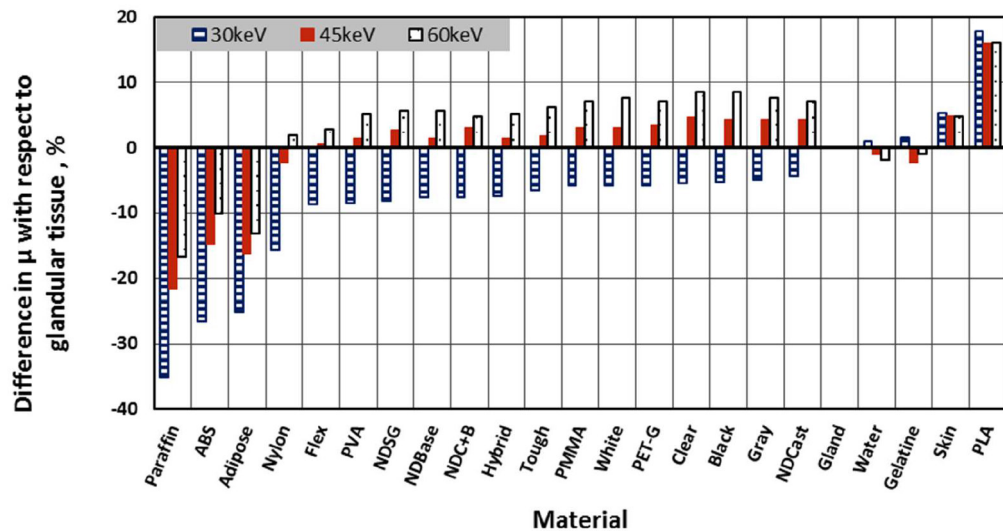
Figure 6. Relative difference in attenuation coefficients μ_{diff} (m_i, *gland*), [%], obtained by measurements at ESRF with respect to the breast glandular tissue for 30 keV, 45 keV and 60 keV.

Figure 7. Relative difference in attenuation coefficients μ_{diff} (m_i, *adipose*), [%], obtained by measurements at ESRF with respect to the breast adipose tissue for 30 keV, 45 keV and 60 keV.

obtaining high-quality solid objects from the resin-based materials turns out to be the best choice for printing glandular tissue.

Similarly to figure 6, figure 7 shows the relative difference of linear attenuation coefficients for the materials with respect to the adipose tissue. As seen from this figure, the ABS material has the closest attenuation coefficient to these of the adipose tissue (especially for 45 keV). Specifically, the absolute value for $|\mu_{diff}|$ calculated for ABS is less than 1.7% and 2.2% for 45 keV and 30 keV, respectively.

The calculated relative difference in μ with respect to the skin tissue for the studied energies is shown figure 8. Here, the resins, Hybrid, PET-G and PVA turn out to be suitable for reproducing the breast skin, especially for energies of 45 keV and 60 keV. In detail, the maximum $|\mu_{diff}|$ for 30 keV for these materials is between 10% and 13%, while for 45 keV and 60 keV the maximum $|\mu_{diff}|$ is less than 4%. From these materials, the most suitable ones for representing skin at 30 keV are gelatin and water, with $|\mu_{diff}|$ less than 4.2%. However, due to the reasons mentioned above, these materials are not preferable for the production of solid-based physical phantoms. Alternative materials are all types of resins. The Clear resin is found to be the choice to represent the skin at 45 keV ($|\mu_{diff}| = 0.13\%$), while at 60 keV the most suitable material turns out to be the Hybrid material ($|\mu_{diff}| = 0.37\%$).
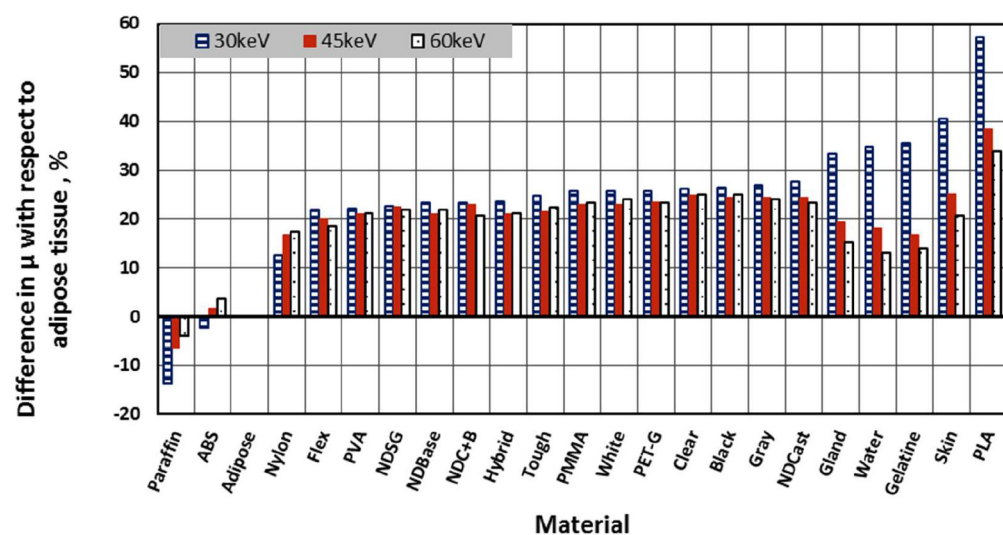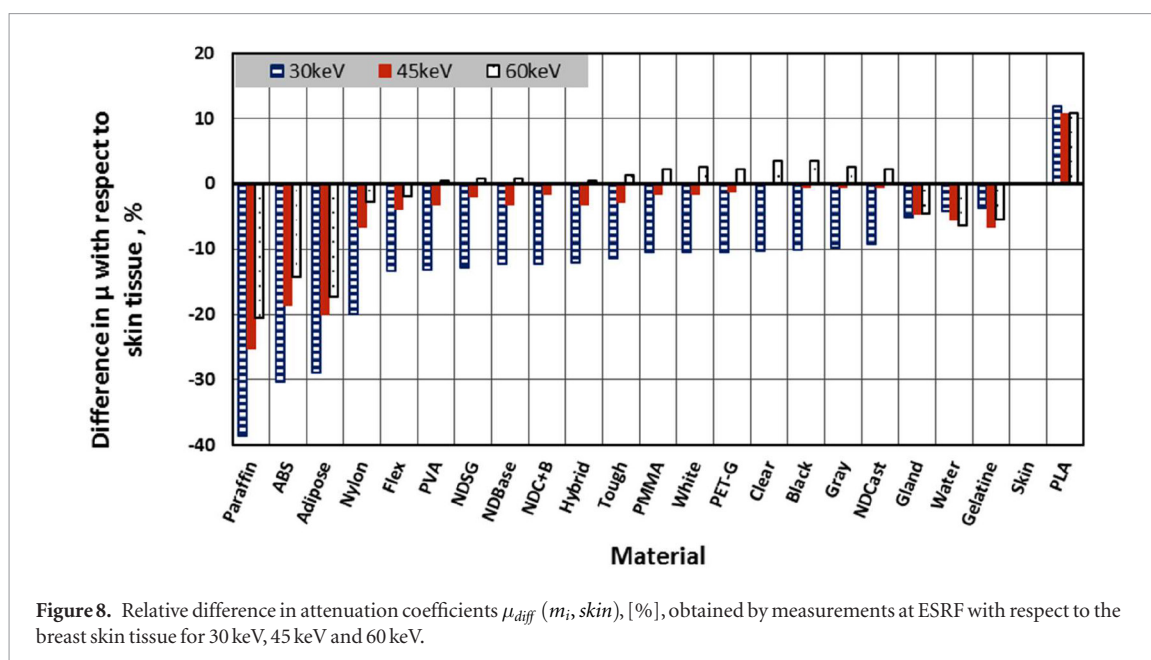
Figure 8. Relative difference in attenuation coefficients μ_{diff} $(m_i, skin)$, [%], obtained by measurements at ESRF with respect to the breast skin tissue for 30 keV, 45 keV and 60 keV.

As expected, the attenuation coefficients are energy-dependent. Creating phantoms for specific energy or narrow energy range may turn to be the right choice in constructing phantoms. For instance, the results in figures 6–8 reveal that a physical breast phantom for 45 keV may be possible to be manufactured from ABS, Flex and Clear, which correspond to adipose, glandular, and skin tissues. Table 3 lists ten choices for suitable substitute materials ranked in order of the square error (equation (7)) for each tissue type and three energies.

The attenuation coefficients of the studied materials depend on the energy, as observed from table 3 and supporting the observation shown in figures 6–8. In order to have realistic contrast, the materials should be selected according to the incident x-ray energy. However, it may be summarized that the resins-based materials, the Nylon, Hybrid and PET-G appear to be most suitable materials to represent both the glandular and skin breast tissues, while ABS represents the adipose tissue well. The decrease in the square error (SE) in table 3 reveals that the increase of the energy results in high degree of similarity between the linear attenuation coefficients, as expected (Byng *et al* 1998).

3.3. Calculated data for δ

To compute delta, the elemental composition of material is needed. The presence of basic elements has been determined by the means of elemental analysis for seven selected materials: the resins Clear, Flex, and Gray as well as PLA, Nylon, PET-G and ABS materials used with the FDM. Their choice was justified mainly based on practical reasons for their eventual use as tissue substitutes, as discussed above. Obtained results (table 4) allowed computing of the refractive decrement index of the materials, which were next compared to those of the reference tissues. The elemental composition of the PMMA, obtained in the same way as for the other materials is also included as a control measurement.

The refractive decrement index δ was calculated for the selected printing materials (from table 4) and resulting values are given in table 5. Reference data for water, PMMA, glandular, adipose tissue and skin are listed in the table, as well. Results show that the δ values of the materials selected to represent the breast tissues for the absorption imaging are higher than the reference δ values for the skin, adipose and gland tissues.

Figure 9 shows the relative difference of the refractive decrement index δ for the selected materials with respect to δ of glandular, adipose and skin tissue. As seen from this figure the relative difference, δ_{diff}, is energy independent.

The results also reveal that materials selected for absorption imaging present different refractive indexes, which are not pertinent for the gland, adipose and skin tissue. As for the linear attenuation coefficients (table 3), we generated all possible ordered triplets out of the studied materials and compared them to the reference triplet of breast tissues. Ten choices for suitable substitute materials are listed in table 6, ranked according to the square error SE_δ (equation (8)):

As seen from table 6 and from the results shown in figure 9, the resin-based materials are most suitable materials to represent the glandular tissue, while the water and ABS are suitable for mimicking the adipose tissue in

Table 3. Suitable materials (in respect to their attenuation properties) for printing breast tissue phantoms ($SE_\mu = \sqrt{\left(\mu_{diff}\left(m_y, m_x\right) - \mu_{diff}\left(gland, adipose\right)\right)^2 + \left(\mu_{diff}\left(m_z, m_x\right) - \mu_{diff}\left(skin, adipose\right)\right)^2}$, [%]).

| | Breast tissues and substitute materials | | | $\mu_{diff},(m_y, m_x)$ | $\mu_{diff},(m_z, m_x)$ | |
keV	m_x	m_y	m_z	%	%	SE_μ, %
30	**Adipose**	**Gland**	**Skin**	**33.5**	**40.7**	
	Paraffin	Nylon	Flex	30.3	41.1	3.2
	Paraffin	Nylon	PVA	30.3	41.5	3.3
	Paraffin	Nylon	NDSG	30.3	41.9	3.4
	ABS	NDCast	Gelatin	30.4	38.5	3.8
	Paraffin	Nylon	NDBase	30.3	42.7	3.8
	Paraffin	Nylon	NDC+B	30.3	42.7	3.8
	Paraffin	Nylon	Hybrid	30.3	43.2	4.0
	ABS	NDCast	Water	30.4	37.7	4.2
	ABS	Gray	Gelatin	29.7	38.5	4.4
	ABS	Black	Gelatin	29.3	38.5	4.7
45	**Adipose**	**Gland**	**Skin**	**19.4**	**25.1**	
	ABS	Tough	Clear	19.5	22.9	2.3
	ABS	Hybrid	Clear	19.1	22.9	2.3
	ABS	NDBase	Clear	19.1	22.9	2.3
	ABS	PVA	Clear	19.1	22.9	2.3
	ABS	NDSG	Clear	20.5	22.9	2.5
	ABS	Flex	Clear	18.1	22.9	2.6
	ABS	Tough	Black	19.5	22.4	2.7
	ABS	Tough	Gray	19.5	22.4	2.7
	ABS	Tough	NDCast	19.5	22.4	2.7
	ABS	NDC+B	Clear	20.9	22.9	2.8
60	**Adipose**	**Gland**	**Skin**	**15.3**	**20.8**	
	ABS	Flex	Black	14.3	20.6	1.0
	ABS	Flex	Clear	14.3	20.6	1.0
	ABS	NDC+B	Black	16.4	20.6	1.2
	ABS	NDC+B	Clear	16.4	20.6	1.2
	ABS	Flex	Gray	14.3	19.6	1.6
	ABS	Flex	White	14.3	19.6	1.6
	ABS	NDC+B	Gray	16.4	19.6	1.7
	ABS	NDC+B	White	16.4	19.6	1.7
	ABS	Hybrid	Black	16.9	20.6	1.7
	ABS	PVA	Black	16.9	20.6	1.7

Table 4. Elemental composition (weighted by fraction) for the candidate printing materials used for skin, gland and adipose.

Material	H	C	N	O[a]	Density g cm^{-3}
PMMA_LAB	0.082 ± 0.002	0.656 ± 0.002		0.262 ± 0.006	1.190
Clear	0.085 ± 0.002	0.648 ± 0.002	0.059 ± 0.002	0.208 ± 0.006	1.180
Flex	0.087 ± 0.002	0.639 ± 0.002	0.044 ± 0.002	0.230 ± 0.006	1.137
Gray	0.084 ± 0.002	0.638 ± 0.002	0.052 ± 0.002	0.226 ± 0.006	1.175
PET-G	0.052 ± 0.002	0.685 ± 0.002	0.012 ± 0.002	0.251 ± 0.006	1.236
PLA	0.058 ± 0.002	0.541 ± 0.002	0.018 ± 0.002	0.383 ± 0.006	1.250
ABS	0.078 ± 0.002	0.862 ± 0.002	0.059 ± 0.002	0.001 ± 0.006	1.019
Nylon	0.097 ± 0.002	0.656 ± 0.002	0.114 ± 0.002	0.133 ± 0.006	1.111

[a] The amount of oxygen was obtained subtracting the sum of all other elements from 1.

Table 5. Refractive decrement indexes, $\delta \times 10^{-7}$.

Material	30 keV	45 keV	60 keV
ABS[a]	2.534	1.126	0.633
Clear[a]	2.954	1.313	0.739
Nylon[a]	2.811	1.249	0.703
Gray[a]	2.939	1.306	0.735
Flex[a]	2.850	1.266	0.712
PET-G[a]	3.001	1.334	0.750
PLA[a]	3.059	1.360	0.765
PMMA[a]	2.978	1.324	0.744
Water[b]	2.566	1.140	0.641
Breast[b]	2.644	1.175	0.661
Adipose[b]	2.385	1.060	0.596
Skin[b]	2.761	1.227	0.690

[a] Compositions are defined in table 4.
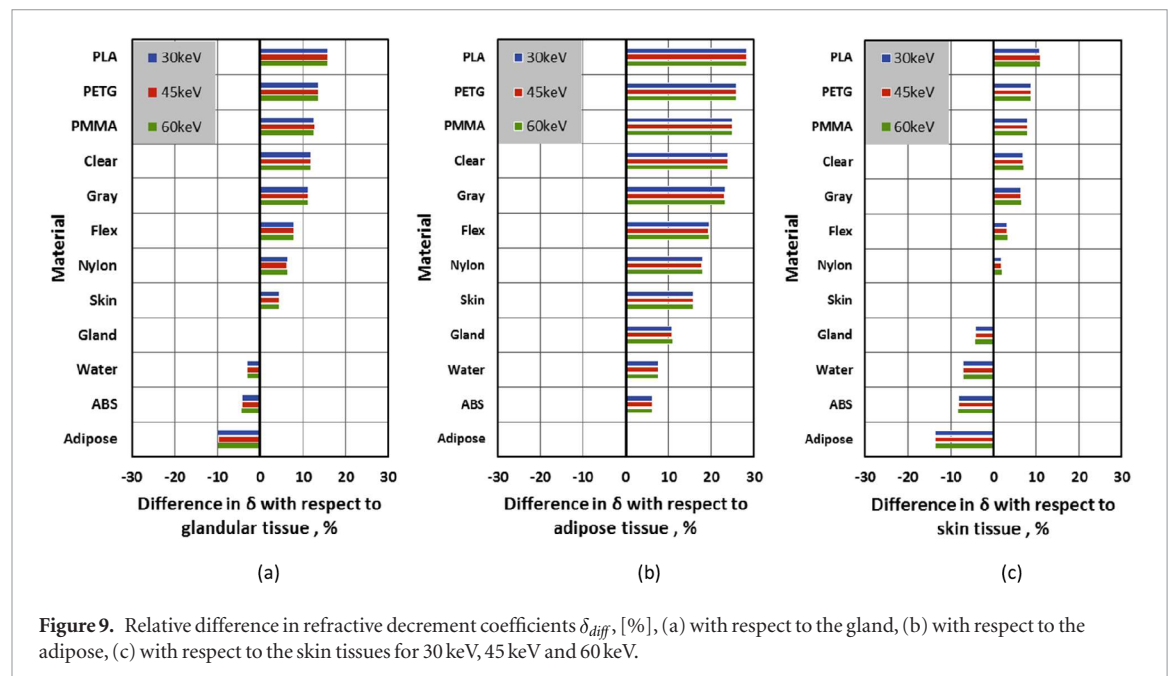
[b] Compositions are defined in table 1.

Figure 9. Relative difference in refractive decrement coefficients δ_{diff}, [%], (a) with respect to the gland, (b) with respect to the adipose, (c) with respect to the skin tissues for 30 keV, 45 keV and 60 keV.

Table 6. Suitable materials (in respect to their refractive properties) for printing breast tissue phantoms
$SE_\delta = \sqrt{\left(\delta_{diff}(m_y, m_x) - \delta_{diff}(gland, adipose)\right)^2 + \left(\delta_{diff}(m_z, m_x) - \delta_{diff}(skin, adipose)\right)^2}$, [%].

keV	Breast tissues and substitute materials			$\delta_{diff}(m_y, m_x)$, %	$\delta_{diff}(m_z, m_x)$, %	SE_δ, %
	m_x	m_y	m_z			
30, 45, 60	**Adipose**	**Gland**	**Skin**	**10.9**	**15.8**	
	ABS	Nylon	Gray	10.9	15.9	0.2
	Water	Flex	PMMA	11.1	16.1	0.4
	Water	Flex	Clear	11.1	15.1	0.7
	ABS	Nylon	Clear	10.9	16.6	0.8
	Water	Flex	PET-G	11.1	16.9	1.2
	Water	Flex	Gray	11.1	14.5	1.3
	Water	Nylon	PMMA	9.6	16.1	1.3
	Water	Nylon	Clear	9.6	15.1	1.5
	ABS	Flex	Gray	12.5	16.0	1.6
	ABS	Nylon	PMMA	10.9	17.5	1.8

terms of refractive index decrement. For instance, resin-based materials are suitable for manufacturing the skin and the glandular tissue, while the adipose tissue may be produced by ABS.

The linear attenuation coefficients were obtained via measurements and validated against calculated data, knowing the elemental composition of the materials. This experimental setup however imposed limitations in respect to inability to precisely measure the refractive decrement index δ. For instance, for PMMA, a differences of 35% is observed between δ calculated for the composition available from NIST and δ obtained from measurements at ESRF. A new experimental approach on synchrotron facility will be studied to precisely measure the δ values of the materials.

This study identified the possible materials to be used for manufacturing the different structures of a breast physical phantom. The results will be employed in the development of a prototype of anthropomorphic physical breast phantom, based on a computational one developed with the *BreastSimulator* (Bliznakova *et al* 2010, 2012). This study showed that adipose may be printed with ABS and used to fill a breast shape from Clear or Hybrid material, and have the glandular tissue printed from Flex resin.

The obtained results may be applicable for lower energies and thus for applications involving planar mammography. Currently, an experimental study is under preparation for defining the attenuation coefficients of the studied materials at lower (<30 keV) energies. While measurements at clinical mammography units are already running, the corresponding ones at synchrotron radiation beamlines are only planned. Monoenergetic synchrotron radiation beams will be used to evaluate these coefficients accurately.

Another study we are performing in parallel is the comparison of simulated mammography images of 3D breast phantoms—prepared from the most suitable tissue-equivalent materials defined in this study—with those obtained when the same phantoms are composed of glandular, adipose and skin breast tissues, also in comparison with patient mammography images (Bliznakova *et al* 2017). The detailed analysis of these images—including evaluation of contrast, fractal dimensions, power spectrum, model observer analysis and others, etc—between the projected materials used for breast tissues and the actual ones will further contribute to determine the applicability of these materials for phantoms design.

4. Conclusions

This study investigated the suitability of several 3D printable plastic materials as tissue substitutes, in the development of physical breast phantoms for attenuation and phase-contrast based x-ray imaging. Twenty-one materials were studied as possible candidates for tissue substitutes for adipose tissue, fibroglandular tissue and skin. Results showed that for absorption imaging resin-based materials, Nylon, Hybrid and PET-G among them are most suitable materials to represent the glandular and skin breast tissue, while ABS represents the adipose tissue well. For phase-contrast imaging, it turns out that ABS combined with resin-based materials to represent the adipose and the glandular tissues, respectively, may be a good combination for the manufacturing of a phantom suitable for this study. An ongoing work is focused on determining the attenuation coefficients of the studied materials at lower energies. Knowledge acquired from this study will be exploited in the manufacturing of breast phantoms dedicated for phase contrast and attenuation breast imaging techniques.

Acknowledgments

Appendix

Table A1. Measured and reference (marked with[a,b,c]) linear attenuation coefficients.

	Compound	$\mu \pm$ standart error, cm^{-1}		
		30 keV	45 keV	60 keV
1	Black	0.353 ± 0.009	0.257 ± 0.006	0.228 ± 0.006
2	Clear	0.352 ± 0.009	0.258 ± 0.006	0.227 ± 0.006
	Clear_LAB[c]	0.346	0.255	0.226
3	Flex	0.340 ± 0.009	0.248 ± 0.006	0.216 ± 0.005
	Flex_LAB[c]	0.336	0.247	0.219
4	Gray	0.354 ± 0.009	0.257 ± 0.006	0.226 ± 0.006
	Gray_LAB[c]	0.346	0.255	0.225
5	Tough	0.348 ± 0.009	0.251 ± 0.006	0.223 ± 0.006
6	White	0.351 ± 0.009	0.254 ± 0.006	0.226 ± 0.006
7	NDBase	0.344 ± 0.009	0.250 ± 0.006	0.222 ± 0.006
8	NDC+B	0.344 ± 0.009	0.254 ± 0.006	0.220 ± 0.006
9	NDCast	0.356 ± 0.009	0.257 ± 0.006	0.225 ± 0.006
10	NDSG	0.342 ± 0.009	0.253 ± 0.006	0.222 ± 0.006
11	Hybrid	0.345 ± 0.009	0.250 ± 0.006	0.221 ± 0.006
12	PET-G	0.351 ± 0.009	0.255 ± 0.006	0.225 ± 0.006
	PET-G_LAB[c]	0.362	0.263	0.231
13	ABS	0.273 ± 0.007	0.210 ± 0.005	0.189 ± 0.005
	ABS[b]	0.294	0.227	0.204
	ABS_LAB[c]	0.272	0.212	0.191
14	Brick	1.150 ± 0.029	0.495 ± 0.012	0.320 ± 0.008
15	Nylon	0.314 ± 0.008	0.241 ± 0.006	0.214 ± 0.005
	Nylon[b]	0.344	0.257	0.228
	Nylon_LAB[c]	0.320	0.240	0.214
16	PVA	0.341 ± 0.009	0.250 ± 0.006	0.221 ± 0.006
17	PLA	0.439 ± 0.011	0.286 ± 0.007	0.244 ± 0.006
	PLA[b]	0.412	0.284	0.246
	PLA_LAB[c]	0.387	0.273	0.238
18	Gelatin	0.378	0.241	0.208
19	Double silicon	0.873 ± 0.022	0.482 ± 0.012	0.338 ± 0.008
20	Paraffin	0.241 ± 0.006	0.193 ± 0.005	0.175 ± 0.004
	Paraffin[a]	0.252	0.202	0.184
21	PMMA	0.351 ± 0.009	0.254 ± 0.006	0.225 ± 0.006
	PMMA[a]	0.361	0.260	0.229
	PMMA_LAB[c]	0.353	0.259	0.229
22	Gland[a]	0.372	0.246	0.210
23	Adipose[a]	0.279	0.206	0.182
24	Skin[a]	0.392	0.258	0.220
25	Water[a]	0.376	0.244	0.206

[a] Theoretical from NIST database.

[b] Theoretical from NIST database, elemental composition is derived from chemical composition based on Alssabbagh *et al* (2017).

[c] Theoretical from NIST database, elemental composition is derived from elemental analysis.

References

Alssabbagh M *et al* 2017 Evaluation of 3D printing materials for fabrication of a novel multi-functional 3D thyroid phantom for medical dosimetry and image quality *Radiat. Phys. Chem.* **135** 106–12

Auweter S D *et al* 2014 X-ray phase-contrast imaging of the breast—advances towards clinical implementation *Br. J. Radiol.* **87** 20130606

Badr S *et al* 2014 Dual-energy contrast-enhanced digital mammography in routine clinical practice in 2013 *Diagn. Interv Imaging* **95** 245–58

Berger M J *et al* 2010 *XCOM: Photon Cross Section Database (Version 1.5)* (Gaithersburg, MD: National Institute of Standards and Technology) http://physics.nist.gov/xcom (Accessed: 26 July 2014)

Bisogni M G *et al* 2007 Experimental study of beam hardening artifacts in photon counting breast computed tomography *Nucl. Instrum. Methods Phys. Res.* A **581** 94–8

Bliznakova K *et al* 2010 Evaluation of an improved algorithm for producing realistic 3D breast software phantoms: application for mammography *Med. Phys.* **37** 5604–17

Bliznakova K *et al* 2012 BreastSimulator: a software platform for breast x-ray imaging research *J. Biomed. Gr. Comput.* **2** 1–14

Bliznakova K *et al* 2016 In-line phase-contrast breast tomosynthesis: a phantom feasibility study at a synchrotron radiation facility *Phys. Med. Biol.* **61** 6243–63

Bliznakova K, Ivanov D, Mettivier G, Russo P, Buliev I and Bliznakov Z 2017 Abstract ID: 66 Monte Carlo and analytical validation of a software breast phantom for X-ray mammography imaging *Phys Medica* **42** 13

Born M and Wolf E 1980 *Principles of Optics* (Oxford: Pergamon)

Bravin A *et al* 2013 X-ray phase-contrast imaging: from pre-clinical applications towards clinics *Phys. Med. Biol.* **58** R1–35

Byng J W *et al* 1998 X-ray characterization of breast phantom materials *Phys. Med. Biol.* **43** 1367–77

Carton A K, Bakic P, Ullberg C, Derand H and Maidment A D 2011 Development of a physical 3D anthropomorphic breast phantom *Med. Phys.* **38** 891–6

Carton A K, Bakic P, Ullberg C and Maidment A D A 2010 Development of a 3D high-resolution physical anthropomorphic breast phantom *Progress in Biomedical Optics and Imaging - Proc. SPIE 2010* **762** 762206

Chen R C *et al* 2010 Measurement of the linear attenuation coefficients of breast tissues by synchrotron radiation computed tomography *Phys. Med. Biol.* **55** 4993–5005

Clark M, Ghammraoui B and Badal A 2016 Reproducing 2D breast mammography images with 3D printed phantoms *SPIE Medical Imaging, 2016* Series 9783 p 9

Dancewicz O L *et al* 2017 Radiological properties of 3D printed materials in kilovoltage and megavoltage photon beams *Phys. Med.* **38** 111–8

Daniaux M *et al* 2015 Dual-energy contrast-enhanced spectral mammography (CESM) *Arch. Gynecol. Obstet.* **292** 739–47

Francescone M A *et al* 2014 Low energy mammogram obtained in contrast-enhanced digital mammography (CEDM) is comparable to routine full-field digital mammography (FFDM) *Eur. J. Radiol.* **83** 1350–5

Ghani M U *et al* 2017 Detectability comparison between a high energy x-ray phase sensitive and mammography systems in imaging phantoms with varying glandular- adipose ratios *Phys. Med. Biol.* **62** 3523–38

Ghani M U *et al* 2018 Detectability comparison of simulated tumors in digital breast tomosynthesis using high-energy x-ray inline phase sensitive and commercial imaging systems *Phys. Med.* **47** 34–41

Hammerstein G R *et al* 1979 Absorbed radiation dose in mammography *Radiology* **130** 485–91

Heine J J and Behera M 2006 Effective x-ray attenuation measurements with full field digital mammography *Med. Phys.* **33** 4350–66

Ikejimba L C, Graff C G, Rosenthal S, Badal A, Ghammraoui B, Lo J Y and Glick S J 2017 A novel physical anthropomorphic breast phantom for 2D and 3D x-ray imaging *Med. Phys.* **44** 407–16

Johns P C and Yaffe M J 1987 X-ray characterisation of normal and neoplastic breast tissues *Phys. Med. Biol.* **32** 675–95

Kalender W A *et al* 2012 High-resolution spiral CT of the breast at very low dose: concept and feasibility considerations *Eur. Radiol.* **22** 1–8

Kiarashi N, Nolte A C, Sturgeon G M, Segars W P, Ghate S V, Nolte L W, Samei E and Lo J Y 2015 Development of realistic physical breast phantoms matched to virtual breast phantoms based on human subject data *Med. Phys.* **42** 4116–26

Lindfors K K *et al* 2008 Dedicated breast CT: initial clinical experience *Radiology* **246** 725–33

Mettivier G and Russo P 2011 Measurement of the MTF of a cone-beam breast computed tomography laboratory scanner *IEEE Trans. Nucl. Sci.* **58** 703–13

Mettivier G *et al* 2017 Evaluation of the BreastSimulator software platform for breast tomography *Phys. Med. Biol.* **62** 6446–66

Poletti M E *et al* 2002 X-ray scattering from human breast tissues and breast-equivalent materials *Phys. Med. Biol.* **47** 47–63

Sarno A, Mettivier G, Di Lillo F, Cesarelli M, Bifulco P and Russo P 2017a Cone-beam micro computed tomography dedicated to the breast *Med. Phys. Eng.* **38** 1449–57

Sarno A, Masi M, Antonelli N, Di Lillo F, Mettivier G, Castriconi R and Russo P 2017b Dose volume distribution in digital breast tomosynthesis: a phantom study *IEEE Trans. Radiat. Plasma Med. Sci.* **1** 322–8

Sarno A *et al* 2015 Dedicated breast computed tomography: basic aspects *Med. Phys.* **42** 2786–804

Sarno A *et al* 2016 Imaging performance of phase-contrast breast computed tomography with synchrotron radiation and a CdTe photon-counting detector *Phys. Med.* **32** 681–90

Sechopoulos I 2013 A review of breast tomosynthesis. Part I. The image acquisition process *Med. Phys.* **40** 014301

Sikaria D *et al* 2016 Second generation anthropomorphic physical phantom for mammography and DBT: incorporating voxelized 3D printing and inkjet printing of iodinated lesion inserts *Medical Imaging 2016: Physics of Medical Imaging* p 9783

Tomal A 2014 Mammography Phantoms *The Phantoms of Medical and Health Physics* ed L DeWerd, M Kissick *Biological and Medical Physics, Biomedical Engineering* (New York: Springer) (https://doi.org/10.1007/978-1-4614-8304-5_8)

White D R *et al* 1978 Epoxy-resin-based tissue substitutes *Med. Phys.* **5** 453–54

Winslow J F *et al* 2009 Construction of anthropomorphic phantoms for use in dosimetry studies *J. Appl. Clin. Med. Phys.* **10** 195–204

Zhao Y Z *et al* 2012 High-resolution, low-dose phase contrast x-ray tomography for 3D diagnosis of human breast cancers *Proc. Natl Acad. Sci. USA* **109** 18290–4

Zhao C, Solomon J, Sturgeon G, Gehm M and Catenacci M *et al* 2017 Third generation anthropomorphic physical phantom for mammography and DBT: incorporating voxelized 3D printing and uniform chest wall QC region *Proc. SPIE 10132, Medical Imaging 2017: Physics of Medical Imaging, 101321Y (9 March 2017)* (https://doi.org/10.1117/12.2256091)